High-SNR Multiple T_2(*)-Contrast Magnetic Resonance Imaging Using a Robust Denoising Method Based on Tissue Characteristics

Taejoon Eo, MS,[1] Taeseong Kim, MS,[1] Yohan Jun, MS,[1] Hongpyo Lee, MS,[1] Sung Soo Ahn, MD,[2] Dong-Hyun Kim, PhD,[1] and Dosik Hwang, PhD[1]*

Purpose: To develop an effective method that can suppress noise in successive multiecho T_2(*)-weighted magnetic resonance (MR) brain images while preventing filtering artifacts.
Materials and Methods: For the simulation experiments, we used multiple T_2-weighted images of an anatomical brain phantom. For in vivo experiments, successive multiecho MR brain images were acquired from five healthy subjects using a multiecho gradient-recalled-echo (MGRE) sequence with a 3T MRI system. Our denoising method is a nonlinear filter whose filtering weights are determined by tissue characteristics among pixels. The similarity of the tissue characteristics is measured based on the l_2-difference between two temporal decay signals. Both numerical and subjective evaluations were performed in order to compare the effectiveness of our denoising method with those of conventional filters, including Gaussian low-pass filter (LPF), anisotropic diffusion filter (ADF), and bilateral filter. Root-mean-square error (RMSE), signal-to-noise ratio (SNR), and contrast-to-noise ratio (CNR) were used in the numerical evaluation. Five observers, including one radiologist, assessed the image quality and rated subjective scores in the subjective evaluation.
Results: Our denoising method significantly improves RMSE, SNR, and CNR of numerical phantom images, and CNR of in vivo brain images in comparison with conventional filters ($P < 0.005$). It also receives the highest scores for structure conspicuity (8.2 to 9.4 out of 10) and naturalness (9.2 to 9.8 out of 10) among the conventional filters in the subjective evaluation.
Conclusion: This study demonstrates that high-SNR multiple T_2(*)-contrast MR images can be obtained using our denoising method based on tissue characteristics without noticeable artifacts.
Level of Evidence: 2

J. MAGN. RESON. IMAGING 2017;45:1835–1845

Magnetic resonance imaging (MRI) is one of the most powerful medical imaging techniques, and it offers high flexibility and multiple imaging with high soft-tissue contrast. Recently, many neuroimaging researchers have used multiple MR brain image sets to analyze fundamental tissue properties. Among these, multiecho T_2(*)-contrast MRI has revealed various tissue properties of the brain, such as myelin content,[1–3] cellular iron uptake,[4,5] susceptibility,[6–8] nerve fiber structure,[9–12] and sources of activation in functional MRI.[13,14]

Unfortunately, these new protocols that acquire multiple images during a restricted scan time have a major limitation: the signal-to-noise ratio (SNR) in each image is lower than in conventional single-echo imaging techniques with low readout bandwidth. Thus, despite the increasing demand for multicontrast MRI, such as multiecho T_2(*)-weighted imaging, an adequate denoising method has yet to be developed (to the best of our knowledge); instead, the noise is removed by conventional filters.

At present, the low SNR problem in MRI is resolved by frequency-selective low-pass filters (LPFs),[15] anisotropic diffusion filters (ADFs),[16–18] bilateral filters,[19] and other conventional filters. Although these filters improve SNR,

View this article online at wileyonlinelibrary.com. DOI: 10.1002/jmri.25477

Received Dec 29, 2015, Accepted for publication Aug 30, 2016.

*Address reprint requests to: D.H., College of Engineering, Yonsei University, 262 Seongsanno, Seodaemun-gu, Seoul, 120-749, Korea. E-mail: dosik.hwang@yonsei.ac.kr

From the [1]School of Electrical and Electronic Engineering, Yonsei University, Seoul, Korea; and [2]Department of Radiology, Yonsei University College of Medicine, Seoul, Korea

TABLE 1. M_0 and T_2 Values Used to Generate Multiecho Images From a Brain Phantom

	CSF	Gray matter	White matter	Fat	Muscle /skin	Skin	Glial matter	MS lesion
M_0 (msec)	1.0	0.86	0.77	1.0	1.0	1.0	0.86	0.76
T_2 (msec)	329	93	70	70	47	329	93	137

most introduce spatial artifacts in the filtered images that impede analysis or diagnosis. LPF introduces blurring artifacts that smoothen the details and boundaries of tissues and induce a partial volume effect.[15] More sophisticated nonlinear filters, such as ADF and bilateral filters, preserve the details and edges of images better than the linear filters while effectively suppressing noise.[20] However, nonlinear processing (eg, diffusion-based smoothing) produces artificial appearances or staircasing artifacts.[21] For these reasons, conventional filters are not widely accepted in many clinical settings.

In conventional filtering methods, the filtering weights are determined by the intensity values of the pixel of interest and its neighbors, which introduces spatial artifacts. Moreover, the single intensity value at the pixel of interest yields no information of the underlying tissue characteristics nor does it distinguish the pixel from its neighbors. Therefore, whether the intensities of some pixels should be averaged or excluded is not easily determined. Noise in the images further complicates the differentiation.

In this study we propose a robust denoising method for multiecho MR images, where the filtering weights are determined depending on the underlying tissue characteristics, not on a single intensity value. This method can efficiently reduce noise while minimizing unwanted spatial artifacts.

Materials and Methods

This study was approved by our Institutional Review Board. Written informed consent was obtained from all human subjects.

Data Acquisition

For in vivo brain imaging, five healthy volunteers (five males, aged 24 ± 1 years) were scanned with a multiecho gradient-recalled-echo (MGRE) sequence using a 3T Siemens MRI system (Siemens Medical Solutions, Erlangen, Germany). The parameters for the MGRE sequence were: first echo time (TE_1) = 5.67 msec, echo spacing (ES) = 5.51 msec, repetition time (TR) = 95 msec, flip angle = 27°, slice thickness = 1.6 mm, bandwidth = 444 Hz/Px, field of view = $215 \times 215\,mm^2$, number of echoes = 16, number of slices = 32, matrix size = $1024 \times 1024 \times 16$ (interpolated from the acquired data with matrix size $512 \times 512 \times 16$), and in-plane resolution = $0.21 \times 0.21\,mm^2$. To reduce the scan time, a generalized autocalibrating partially parallel acquisition[22] was applied to the MGRE sequence with an acceleration factor of 2. The total acquisition time was 15 minutes 30 seconds. To demonstrate the effectiveness of the proposed denoising method, the resulting 16 image sets with different T_2^* weightings were denoised by the proposed method and several conventional filters. All steps of the image processing, including filtering and region of interest (ROI) measurement, were performed using MatLab (MathWorks, Natick, MA).

Simulation of Synthetic Data

For quantitative evaluation, we acquired multiple T_2-weighted images of an anatomical brain phantom with multiple sclerosis (MS) lesions from BrainWeb.[23–25] For simplicity, a temporal decay signal of each pixel was generated by a monoexponential model, assuming that each voxel comprises a single compartment.[26] The brain phantom was comprised of eight types of tissues. Table 1 lists the M_0 and T_2 values (referred from BrainWeb) used to generate the monoexponential decay signals.

The multiple T_2-weighted images were generated under the following imaging parameters: infinite TR (full recovery), $TE_1 = 5$ msec, ES = 5 msec, number of echoes = 20, and matrix size = $181 \times 217 \times 20$. The temporal decay signal of each pixel was calculated as follows:

$$I(\vec{x}, TE_i) = M_0(\vec{x}) \times e^{-\frac{TE_i}{T_2(\vec{x})}},\ TE_i = 5, 10, 15, \ldots, 95, 100\ \text{ms} \quad (1)$$

where $\vec{x}$ is a pixel position; TE_i is the i-th TE; $M_0(\vec{x})$ and $T_2(\vec{x})$ are the M_0 and T_2 values of a tissue at $\vec{x}$, respectively; and $I(\vec{x}, TE_i)$ is the intensity of $\vec{x}$ at TE_i. The simulation data were superimposed with white Gaussian noise with a standard deviation of 9% of the pixel intensity of the brightest tissue cerebrospinal fluid (CSF) at the first echo time. The left, center, and right panels of Fig. 1 show T_2-weighted images at TE = 10, 50, and 100 msec, respectively. Because each tissue has a different T_2 decay rate, all T_2-weighted images show various contrasts.

Neighborhood Filtering

A neighborhood filter is any filter that restores a pixel by taking the weighted combination of the intensities of largely "similar" pixels.[27] Typically, similarities among pixels depend on the spatial information, intensity information,[19,28] and patch or vector information[27] in an image.

An early example of a neighborhood filter is the Yaroslavsky filter,[28] which weighs the intensity similarities of the pixels close to the reference pixel while assigning zero weights to more distant pixels. The intensity similarity is defined as a Gaussian function:

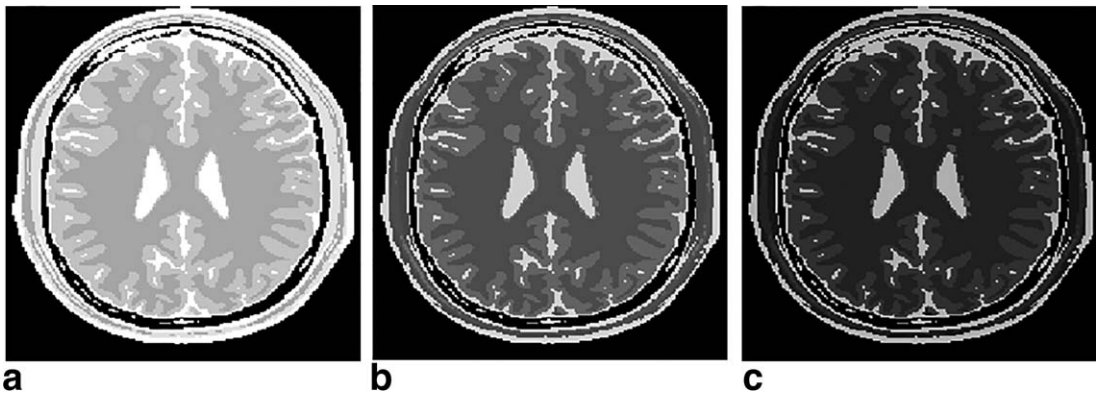

FIGURE 1: Multiple T_2-weighted images for numerical brain phantom in noiseless simulation studies with: (a) TE = 10 msec, (b) 50 msec, (c) 100 msec.

$$s_I(\vec{x},\vec{x_r}) = e^{-\frac{1}{2}\left(\frac{|I(\vec{x})-I(\vec{x_r})|}{\sigma_I}\right)^2}, \quad (2)$$

where $\vec{x_r}$ and $\vec{x}$ are the positions of the reference pixel and another pixel in the image, respectively. $I(\vec{x})$ and $I(\vec{x_r})$ denote the intensities at $\vec{x}$ and $\vec{x_r}$, respectively. σ_I is a filtering parameter (the standard deviation of the Gaussian function), and $S_I(\vec{x},\vec{x_r})$ is the intensity similarity between $\vec{x}$ and $\vec{x_r}$. When filtering $\vec{x_r}$ by the Yaroslavsky filter, $\vec{x}$ is weighted as follows:

$$w_{yar}(\vec{x},\vec{x_r}) = \begin{cases} s_I(\vec{x},\vec{x_r}) & if\ |\vec{x}-\vec{x_r}| \le R \\ 0 & if\ |\vec{x}-\vec{x_r}| > R' \end{cases} \quad (3)$$

where $|\vec{x}-\vec{x_r}|$ is the spatial distance between $\vec{x}$ and $\vec{x_r}$, and R is a spatial distance threshold that identifies the spatially neighboring pixels.

A more recent neighborhood filter is the bilateral filter,[19] which evaluates both spatial and intensity similarities. Similar to the intensity similarity, the spatial similarity is denoted by a Gaussian function:

$$s_s(\vec{x},\vec{x_r}) = e^{-\frac{1}{2}\left(\frac{|\vec{x}-\vec{x_r}|}{\sigma_s}\right)^2}, \quad (4)$$

where σ_S is the standard deviation of the Gaussian function. In the bilateral filtering of $\vec{x_r}$, $\vec{x}$ is weighted by:

$$w_{bi}(\vec{x},\vec{x_r}) = s_s(\vec{x},\vec{x_r})s_I(\vec{x},\vec{x_r}) \quad (5)$$

Finally, the pixel intensity denoised by the neighborhood filters is expressed as a weighted combination of the intensities of pixels in the image, denoted by Ω:

$$I_{NH}(\vec{x_r}) = \frac{\sum_{\vec{x}\in\Omega} w_{NH}(\vec{x},\vec{x_r})I(\vec{x})}{\sum_{\vec{x}\in\Omega} w_{NH}(\vec{x},\vec{x_r})} \quad (6)$$

where $w_{NH}(\vec{x},\vec{x_r})$ is the weighting value of a generalized neighborhood filter. In the Yaroslavsky and bilateral filters, this parameter is denoted as $w_{yar}(\vec{x},\vec{x_r})$ and $w_{bi}(\vec{x},\vec{x_r})$, respectively.

Denoising Method Based on Tissue Characteristics

The proposed denoising method borrows the concept of conventional neighborhood filters; that is, it restores a pixel by taking the weighted combination of pixels with large similarities. However, because the filtering weights are determined from the spatial information and/or intensities of the pixels while disregarding their underlying tissue characteristics, these filters introduce spatial artifacts, such as blurring, flattening, and mottling. To prevent these spatial artifacts while reducing noise and retaining the underlying tissue properties, we propose filtering weights based on similar tissue characteristics among the pixels. The tissue characteristics of a pixel manifest as different decay patterns in the temporal decay signals of successive multiecho T_2(*) MR images.[29] The temporal decay signal from each pixel exhibits tissue-dependent characteristics, such as proton density, T_1, and the T_2 or T_2^* decay rate. Therefore, whether two pixels have similar tissue characteristics can be determined by checking the similarity between their temporal signal patterns. Furthermore, weighting the proposed denoising method excludes spatial similarity because pixels with similar tissue characteristics can exist at any position in the image. In fact, pixels distant from the reference pixel can be weighted more heavily in the proposed denoising method, thus greatly enhancing SNR. In order to identify the similarity of the tissue characteristics between two pixels, we compute the intertissue distance between the pixels:

$$D(\vec{x},\vec{x_r}) \triangleq \sum_{i=1}^{N} |I(\vec{x},TE_i) - I(\vec{x_r},TE_i)|^2 \quad (7)$$

where TE_i is the i-th TE and N is the total number of TEs. $I(\vec{x},TE_i)$ and $I(\vec{x_r},TE_i)$ denote the intensities of pixel $\vec{x}$ at TE_i and pixel

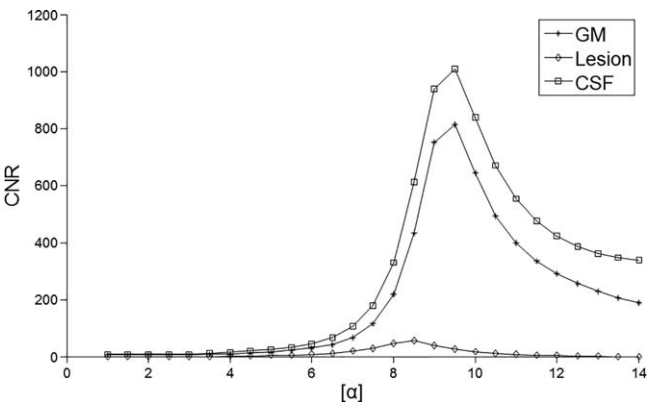

FIGURE 2: CNR values of three different tissues (GM, lesion, and CSF) for simulation data. Threshold value is $th = \alpha\sigma_b$, where σ_b is the standard deviation of background noise.

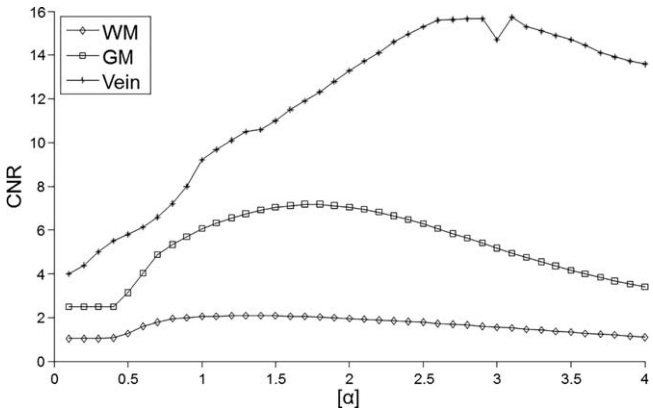

FIGURE 3: CNR values of three different tissues (WM, GM, and vein) with different threshold values for in vivo data.

$\vec{x_r}$ at TE_i, respectively. $D(\vec{x}, \vec{x_r})$ is the intertissue distance between $\vec{x}$ and $\vec{x_r}$. Furthermore, when filtering pixel $\vec{x_r}$ pixel $\vec{x}$ is weighted as:

$$w(\vec{x}, \vec{x_r}) = \begin{cases} 1 & if\ D(\vec{x}, \vec{x_r}) \le th \\ 0 & if\ D(\vec{x}, \vec{x_r}) > th \end{cases} \quad (8)$$

where th is the threshold value that determines whether $\vec{x}$ has tissue characteristics similar to $\vec{x_r}$. This parameter determines the degree of filtering, which depends on the noise or signal level and number of TEs. The weighting value $w(\vec{x}, \vec{x_r})$ is set to 1 or 0. Alternatively, $w(\vec{x}, \vec{x_r})$ can be given by a Gaussian function of $D(\vec{x}, \vec{x_r})$, as follows:

$$w(\vec{x}, \vec{x_r}) = s_{tc}(\vec{x}, \vec{x_r}) = e^{-\frac{1}{2}\left(\frac{D(\vec{x}, \vec{x_r})}{\sigma_{tc}}\right)^2}, \quad (9)$$

where $s_{tc}(\vec{x}, \vec{x_r})$ is the tissue-characteristics similarity between $\vec{x}$ and $\vec{x_r}$, and σ_{tc} is the standard deviation of the Gaussian function. Both weighting functions yielded similar denoising performance in our preliminary studies. Therefore, in real experiments we adopted the weighting function shown in Eq. [8] for simpler implementation and faster processing. The normalization factor or number of pixels with similar tissue characteristics to $\vec{x_r}$ was obtained as:

$$n(\vec{x_r}) = \sum\nolimits_{\vec{x} \in \Omega} w(\vec{x}, \vec{x_r}), \quad (10)$$

where Ω is all image pixels. The denoised pixel intensity of $\vec{x_r}$ at TE_i was obtained as a weighted combination of the pixel intensities in the same-TE image:

$$I_d(\vec{x_r}, TE_i) = \frac{\sum_{\vec{x} \in \Omega} w(\vec{x}, \vec{x_r}) I(\vec{x}, TE_i)}{n(\vec{x_r})} = \sum\nolimits_{\vec{x} \in \Omega} w_n(\vec{x}, \vec{x_r}) I(\vec{x}, TE_i) \quad (11)$$

where $w_n(\vec{x}, \vec{x_r})$ is the weighting value normalized by $n(\vec{x_r})$. Finally, the denoised multiecho images were obtained with the pixel-wise process of Eq. [11] for all pixels in the images.

Determination of Threshold Value

In order to choose the optimal threshold value th in Eq. [8], we analyzed the filtering results for different threshold values. Figure 2

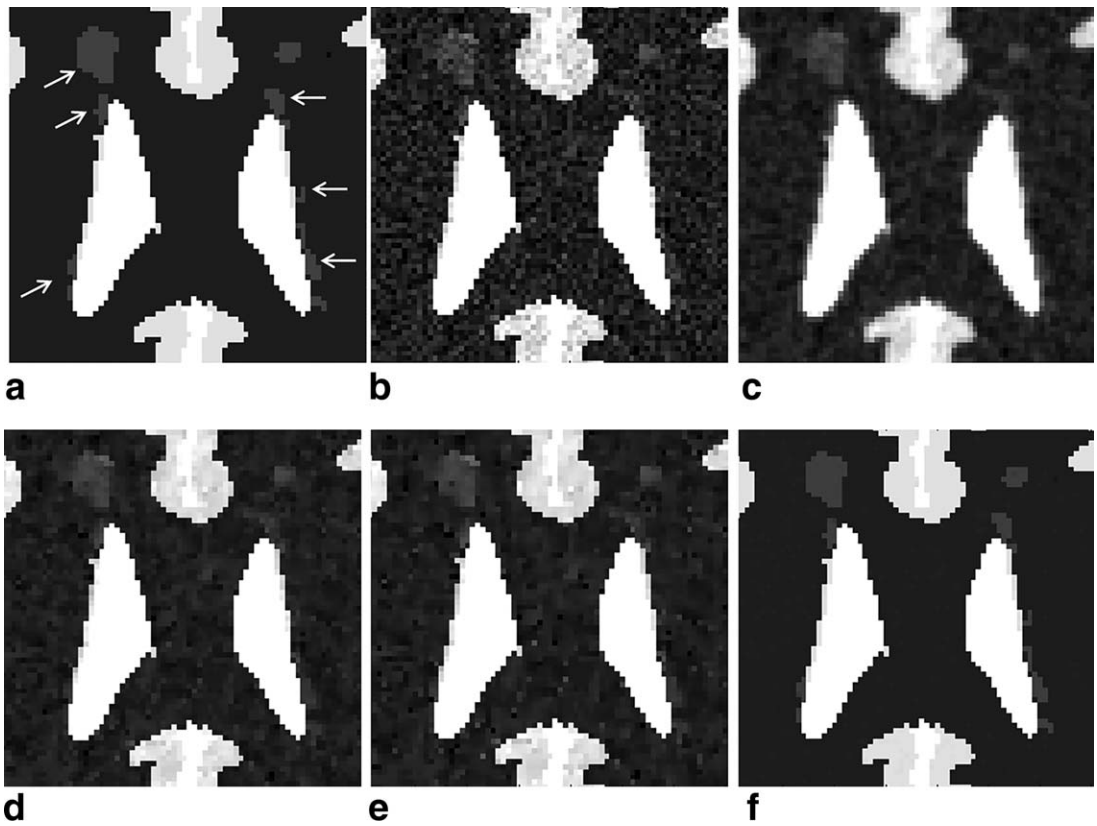

FIGURE 4: Denoising results of simulation studies: (a) magnified image for original image at TE = 50 msec, (b) magnified noisy image, (c) images denoised by LPF, (d) ADF, (e) bilateral filter, (f) proposed denoising method. White arrows in (a) point to eight lesions.

shows the CNR values of the simulation data with three different tissues (gray matter [GM], lesion, and CSF) and threshold values $th = \alpha\sigma_b$, where σ_b is the standard deviation of the background noise. We calculated mean CNR over all TEs (Fig. 2). CNR for GM and lesion reached its maxima at approximately $\alpha = 9.5$, and CSF reached its maxima at approximately $\alpha = 8.5$. We chose $\alpha = 9.5$ for our simulation experiment.

Figure 3 shows the CNR values of three different tissues (WM, GM, and vein) with different threshold values at in vivo data. CNR for WM reached its maxima at approximately $\alpha = 1.0$–1.8. CNR for GM reached its maxima at approximately $\alpha = 1.6$–1.8. CNR for vein reached its maxima at approximately $\alpha = 2.5$–2.8. We focused on improving the soft-tissue contrasts, and therefore we chose α of 1.8 for our in vivo experiment.

Comparison With Conventional Spatial Filters

The performance of the proposed denoising method was compared with those of three conventional filters: Gaussian LPF, ADF, and bilateral filter. The parameters of each conventional filter were selected by evaluating the CNR performance in the repetitive experiments with different parameter values such that each conventional filter could produce its best CNR results. For LPF, the standard deviation of the Gaussian function and kernel size were set to 0.6 and 7×7, respectively, in the simulation experiment and 1.2 and 11×11, respectively, in the in vivo experiment. Parameter κ for ADF was set to 0.02 and 0.03 in the simulation and in vivo experiments, respectively. For both experiments, the iteration number was set to 8. For the bilateral filter, the kernel size and σ_S were set to 20×20 and 1.1, respectively, in both experiments, whereas σ_I was set to 0.13 and 0.6 in the simulation and in vivo experiments, respectively.

For the quantitative evaluation, the RMSE values were compared in simulation studies and the CNR values were compared in both simulation and in vivo studies. RMSE between the denoised and true images was calculated as the l_2 difference between the two images:

$$RMSE = \|I_{true} - I_d\|_2 \tag{12}$$

where I_{true} and I_d denote a set of pixel intensities in the true and denoised images, respectively. SNR of ROI a was calculated as follows:

$$\mathrm{SNR}_a = \frac{\mu_a}{\sigma_a} \tag{13}$$

where μ_a and σ_a are the mean value and standard deviation of the pixels in ROI a, respectively. CNR between foreground tissue f and background tissue b was calculated as follows:

$$CNR_{f,b} = \frac{|\mu_f - \mu_b|}{\sigma_b} \tag{14}$$

where μ_f and μ_b are the mean pixel values in the ROIs of f and b, respectively. σ_b is the standard deviation of the pixel intensities for ROI of b.

For the subjective evaluation, five observers, including one radiologist, performed a blind image quality assessment[30] for the denoised images in terms of structure conspicuity and naturalness. It was demonstrated that subjective naturalness correlates highly with image distortions and noise in optics-image assessments.[31] Therefore, we used this subjective metric to evaluate artifacts and noise in our experiments. All scores range from 1 (very bad) to 10 (very good). Mean opinion scores (MOS), commonly used in subjective evaluations, were obtained by taking an average of the scores rated by all observers.[30,31]

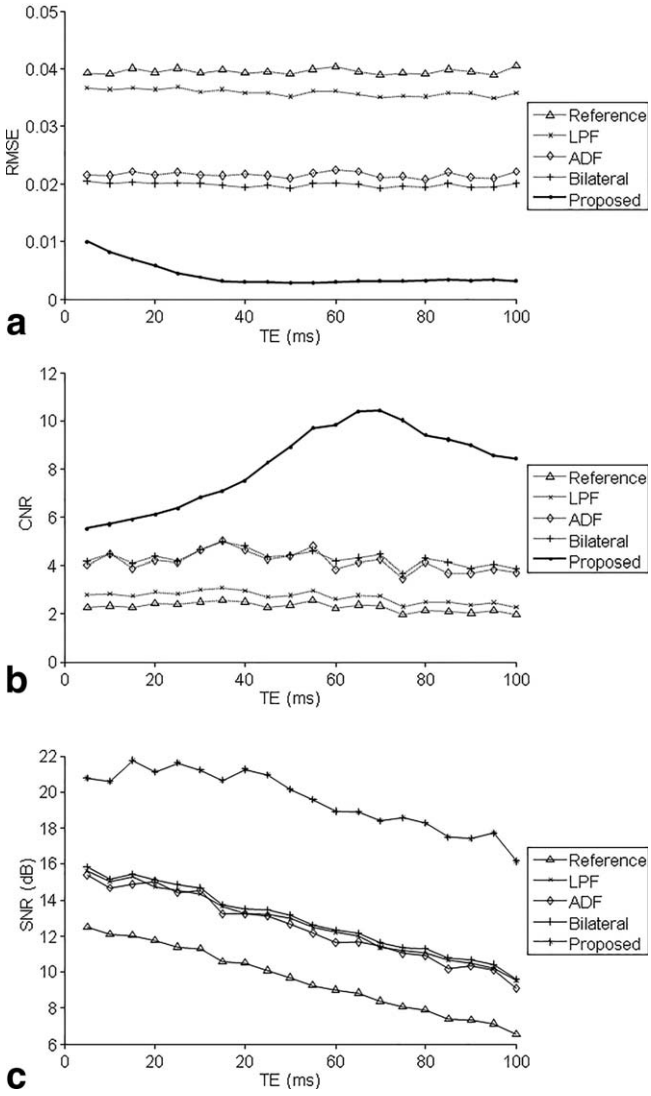

FIGURE 5: Plots for: (a) RMSE, (b) CNR between lesions and background tissues, (c) SNR at a region of WM.

Results

Simulation Studies

Figure 4 shows the denoising results from the simulation studies of the true image (Fig. 4a) and noisy image (Fig. 4b) at TE = 50 msec extracted from the synthetic multiecho dataset.

Figure 5 shows the plots of RMSE (Fig. 5a), CNR between the lesions and background tissues (Fig. 5b), and SNR at a region of WM (Fig. 5c) for the images shown in Fig. 4 as functions of TE. The CNR values were averaged

TABLE 2. Quality Evaluation of Simulation Data. RMSE, CNR, SNR, and MOS for Lesion Conspicuity at Three Echo Times (10, 50, and 90 msec)

TE (msec)	Evaluation metrics	Noisy	LPF	ADF	Bilateral	Proposed method
10	RMSE	0.0392	0.0365	0.0215	0.0201	0.0083
	CNR	2.375	3.669	3.880	4.247	7.058
	SNR	12.137	15.042	14.688	15.174	20.604
	Lesion conspicuity	6.4	7.0	7.0	7.4	9.4
50	RMSE	0.0392	0.3525	0.0211	0.0193	0.0029
	CNR	2.367	4.394	4.378	4.575	8.037
	SNR	9.690	12.971	12.675	13.133	20.118
	Lesion conspicuity	7.6	7.4	7.8	7.0	9.2
90	RMSE	0.0396	0.3573	0.0212	0.0195	0.00331
	CNR	2.217	4.445	3.997	4.049	7.270
	SNR	7.372	10.445	10.312	10.665	17.399
	Lesion conspicuity	7.0	6.2	6.0	6.6	8.2

over the eight CNR values between the eight lesions and their background tissues. According to the RMSE graph (Fig. 5a), the proposed denoising method results in the lowest RMSE, demonstrating that it substantially reduces noise and most accurately restores the original image among the tested methods. The CNR graph (Fig. 5b) shows that the proposed denoising method preserves the boundaries between lesions and WM the best. The SNR graph (Fig. 5c) indicates that the proposed denoising method shows the highest SNRs for all TEs.

Table 2 lists RMSE, CNR, SNR, and subjective MOS for lesion conspicuity at three different echoes (10, 50, 90 msec). Although the conventional filters improve the three objective metrics compared with the noisy images, their lesion conspicuity scores are similar to, or rather less than, those of the original noisy images. In contrast, our denoising method receives the highest lesion conspicuity scores and the best performance in those three objective metrics.

Figure 6 shows the effects of ES and echo number of multiecho images on the denoising performances of the proposed method. RMSE exponentially decreases as the number of echoes increase from 1 (which represents a single-contrast image set). Notably, at only two echoes, RMSE is lower after denoising by the proposed method than by the conventional spatial filters. At four echoes, RMSE in the proposed method decreases to 1/4 of the noise RMSE. Varying ES at 1, 3, and 5 msec exerts scant effect on RMSE at a given number of echoes. However, longer ES (10 and 20 msec) degrades RMSE because the images acquired at long TEs, such as 200 msec, contain no meaningful signal components.

In Vivo Experiments

Figure 7 shows the original noisy image (Fig. 7a), image denoised with the proposed filter (Fig. 7b), and magnified image of ROI B shown in Fig. 7b (Fig. 7c). The six regions for calculating CNR between GM and WM are presented in Fig. 7a,b. The delineated regions of GM and WM regions (these ROIs are used in the CNR calculations of all denoised images) are shown in Fig. 7c. Here, ROIs for GM (solid line) and WM (dashed line) are spaced closely to assess the boundary blurring effects caused by the denoising process.

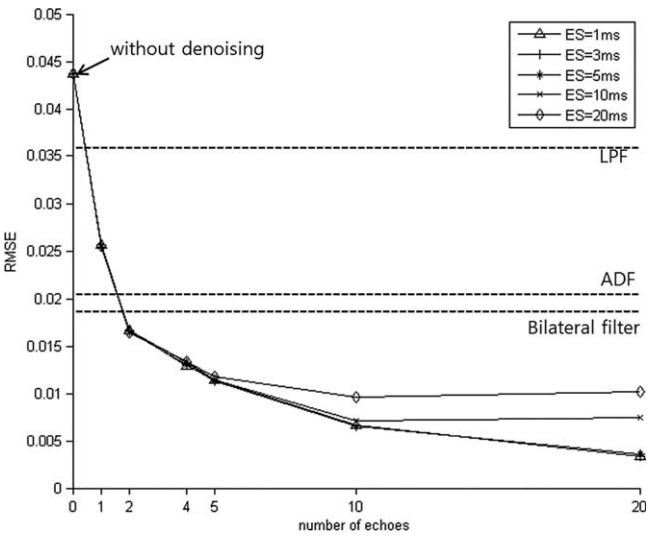

FIGURE 6: RMSE for proposed denoising method versus number of echoes of multiecho MR images.

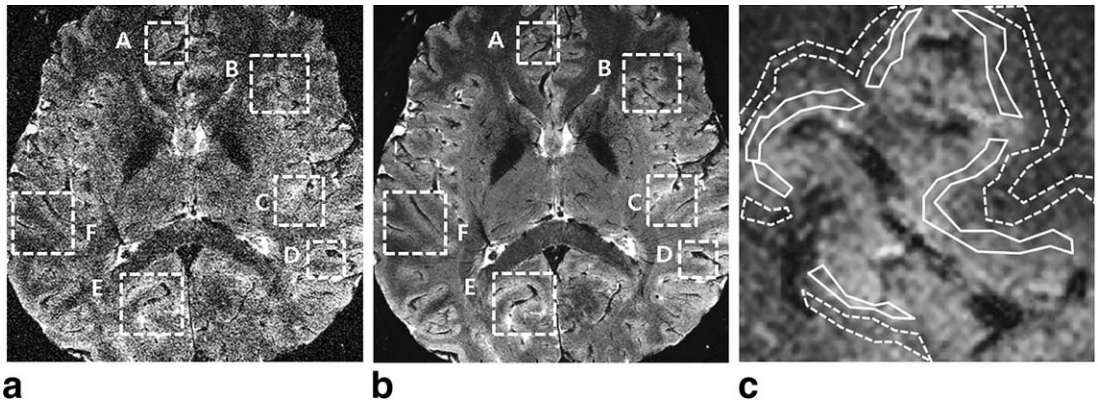

FIGURE 7: (a) Original noisy image, (b) image denoised by proposed filter, (c) magnified image of ROI B in (b). Delineated regions of GM (solid line) and WM (dashed line) are shown in (c).

Figure 8 shows the magnified images in ROI B of Fig. 7 at two TEs: 22.2 msec (row a) and 66.28 msec (row b). This figure shows, from left to right, the original noisy image and images denoised by various filtering methods.

Figure 9 shows CNR between GM and WM calculated in the six ROIs of Fig. 7 at short and long TE (22.2 msec (Fig. 9a) and 66.28 msec (Fig. 9b), respectively). Among the tested denoising methods, the proposed method achieved the highest CNR for all ROIs and both TEs, thus confirming that this method best preserves the contrast between GM and WM with substantial noise reduction.

Table 3 lists the mean CNR values and two subjective scores for the images in Fig. 8. In this numerical evaluation, the proposed denoising method shows the highest CNR at both short and long echo times, which suggests that the boundaries between GM and WM are most effectively preserved by the proposed method. In the subjective evaluation, the proposed method also receives the highest scores for GM conspicuity and naturalness at both echo times.

Figure 10 shows CNRs averaged over the six ROIs for each of 16 echo times. The standard deviation values of the six CNR values are also depicted with error bars. For all echo times, the proposed denoising method consistently achieves the highest CNR among all denoising methods.

In order to check the statistical significance of the CNR improvement of the proposed denoising method, *P*-values were calculated by a paired *t*-test between 16 echoes of CNR values from the proposed denoising method, and the CNR values from each of the other cases (original noisy, LPF, ADF, and bilateral). The respective four *P*-values $P_{\text{P-N}}$, $P_{\text{P-L}}$, $P_{\text{P-A}}$, and $P_{\text{P-B}}$ are 0.0023, 0.0037, 0.0043, and 0.0048. This statistical test confirms that the proposed denoising method is superior to the other denoising methods in CNR performance with high statistical significance ($P < 0.005$).

Figure 11 presents the denoising results of four different subjects (subjects 2–5) at TE = 38.7 msec. The figure shows the original noisy images (row a) and their denoised images by the proposed denoising method (row b). The

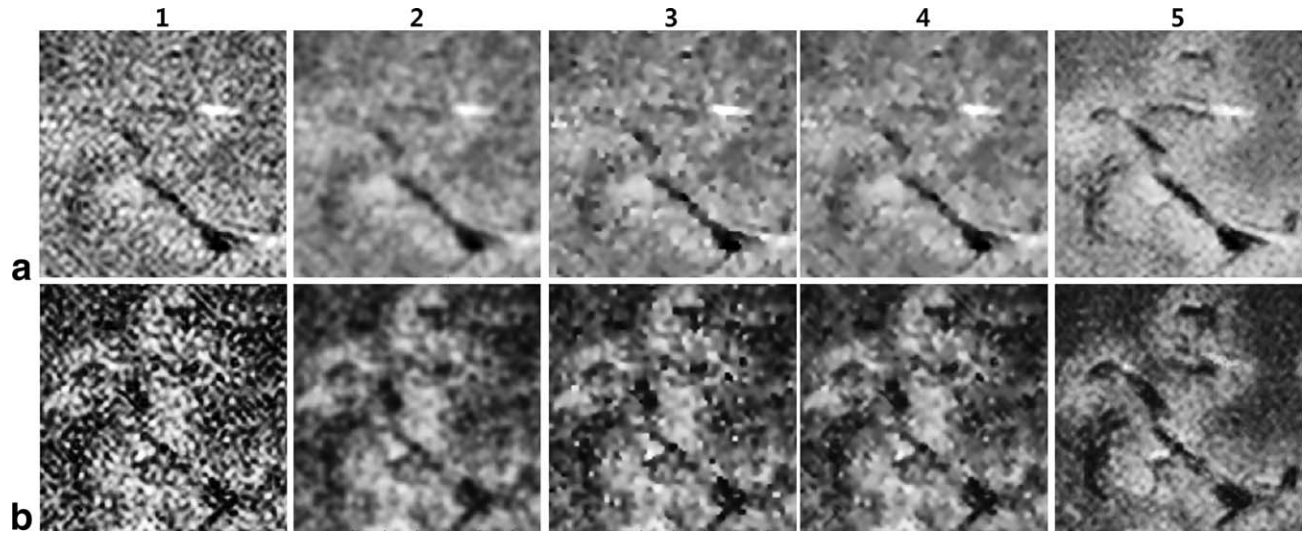

FIGURE 8: Comparison of magnified images in ROI B in Fig. 7 at TE = 22.2 msec (row a) and 66.28 msec (row b). Left to right: original noisy image, images denoised by LPF, ADF, bilateral filter, and proposed denoising method.

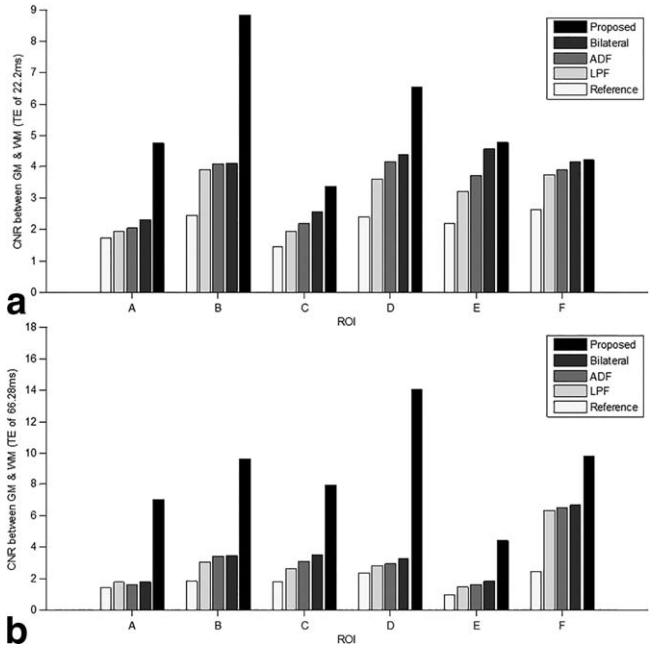

FIGURE 9: CNR between GM and WM at given TE in six ROIs: (a) TE = 22.2 msec, (b) TE = 66.28.

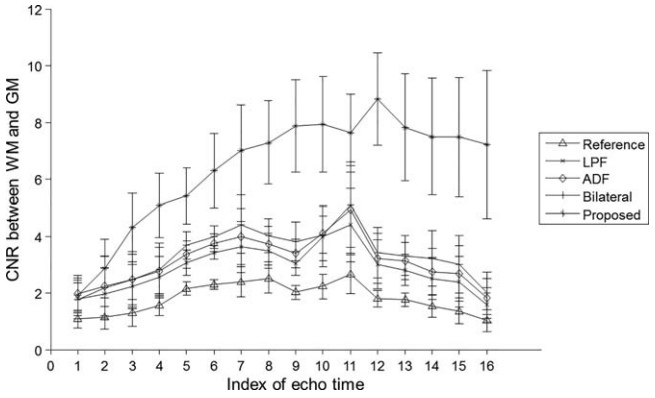

FIGURE 10: CNR between GM and WM averaged over six ROIs. Standard deviation is depicted with error bars.

images in row b were denoised using the same threshold value used to denoise the images in Fig. 7. Notwithstanding the different subjects, the same threshold value results in reasonable denoising performance when the body part and sequence specifications are the same.

Figure 12 compares the denoising results with the conventional filters for the images of subjects 4 and 5 shown in columns 3 and 4 of Fig. 11, respectively. Subjective evaluations were performed for the conspicuity of subthalamic nucleus (STN) and red nucleus (RN) in these images, and the resulting MOS values are presented in Table 4. The images denoised with the proposed method receive the highest STN/RN conspicuity scores.

Discussion

High-SNR multicontrast $T_2(*)$-weighted brain imaging that uses a robust denoising method was proposed. The proposed denoising method is adapted from neighborhood filters whose filtering weights are determined by the intensity or geometric similarity among pixels in a single 2D image.[19,27,28] However, it has been reported that conventional neighborhood filters introduce staircasing artifacts and artificial patterns on images.[21,27] To overcome such problems, our denoising method extends the intensity or geometric similarity to tissue-characteristics similarity by exploiting the third dimension of multiecho MR data, which is the echo time. Tissue-characteristics similarities, which determine the filtering weights of our denoising method, were obtained using Euclidean distance among temporal signals of pixels.

The effectiveness of our denoising method was demonstrated by numerical and subjective evaluations in both simulation and in vivo experiments. Our denoising method significantly improved RMSE, SNR, and CNR in the numerical evaluation ($P < 0.005$), whereas it showed better MOS of the structure conspicuity (8.2 to 9.4 out of 10) and naturalness (9.2 to 9.8 out of 10) compared with the conventional filters in the subjective evaluation. Other recent studies on denoising MR images have also evaluated their proposed spatial filters by measuring SNR,[32,33] RMSE,[33,34] and MOS.[33,34] The spatial filters of the conventional studies showed 1.20–1.68-fold,[32,33] 1.34–1.62-fold,[33,34] and 1.16–1.52-fold[33,34] improvement in SNR, RMSE, and MOS, respectively, compared with the results of a bilateral filter. Meanwhile, our denoising method

TABLE 3. Mean CNR Values and Two Subjective Scores for Images in Fig. 7

TE (ms)	Evaluation metrics	Original noisy	LPF	ADF	Bilateral	Proposed
22.2	Mean CNR	1.544	2.734	2.850	2.983	5.085
	GM conspicuity	5.4	6.0	7.2	7.0	8.8
	Naturalness	3.8	5.8	4.0	5.4	9.2
66.28	Mean CNR	1.020	1.793	1.878	1.913	5.634
	GM conspicuity	4.2	5.6	6.2	7.0	9.4
	Naturalness	3.8	5.8	4.0	7.3	9.8

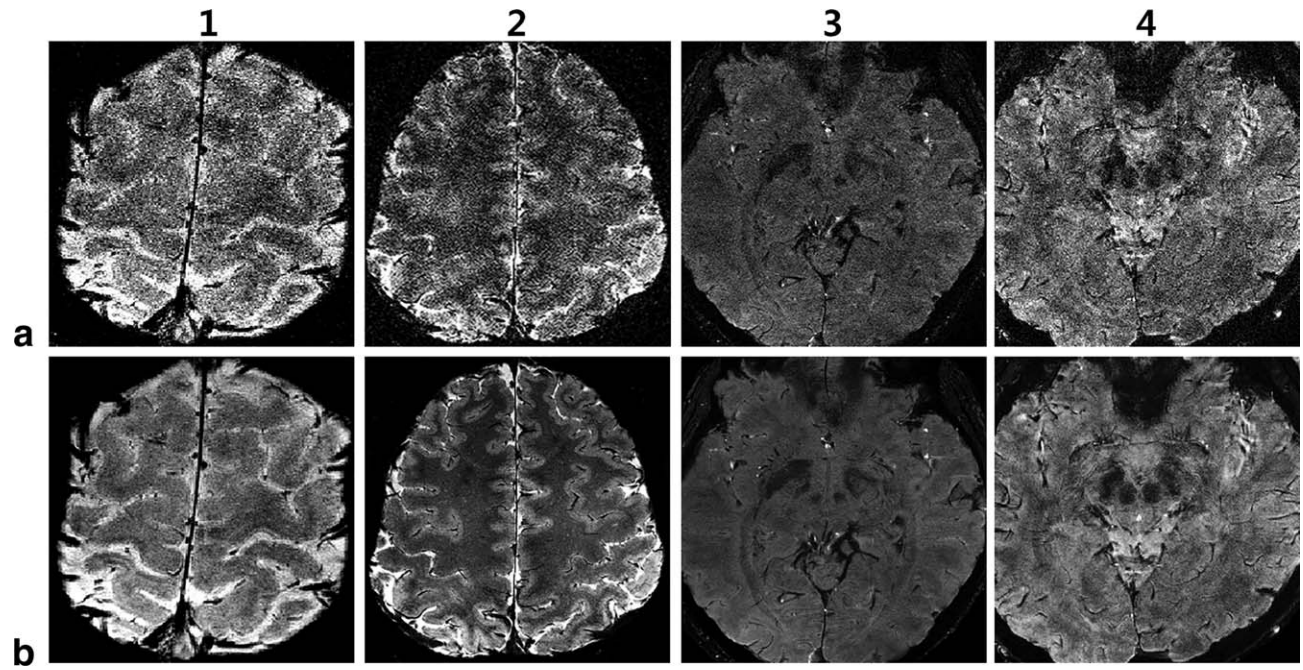

FIGURE 11: Denoising results of four different subjects at TE = 38.7 msec. Original noisy images (row a) and images denoised by proposed method (row b) are shown.

showed averages of 2.08-fold, 6.72-fold, and 2.42-fold improvements. Although a direct comparison of our results with the reported literature values would be difficult because the subjects, noise level, and sequence parameters are different among the studies, our denoising method showed higher improvement in the three metrics. However, the current evaluation has some limitations in generalizing the effectiveness of our denoising method for multiecho brain imaging for two reasons. First, our denoising method was only applied to in vivo images acquired with the same acquisition parameters. Therefore, the high performance of our proposed method in this study is not guaranteed for multiecho images acquired with other acquisition parameters. Second, we used only normal-brain images that do not include pathological tissues. The denoising performance for pathological tissues might be different with normal tissues because the former, such as brain tumors and hemorrhage tissues, have different tissue characteristics compared with the latter.[35,36] Consequently, in order to generalize our denoising method for multiecho brain imaging, additional experiments for the images acquired with the sequence parameters commonly used in clinical settings and various pathological in vivo brain images are required.

Our denoising method has limitations that need to be addressed in future studies. The first limitation is that, because averaging is performed over a number of pixels with similar tissue characteristics in the image dataset, SNR improves less in tissues with small populations (such as veins) than in more-populated tissues, such as GM and WM. Similarly, B_1 or B_0-bias field distortion could degrade

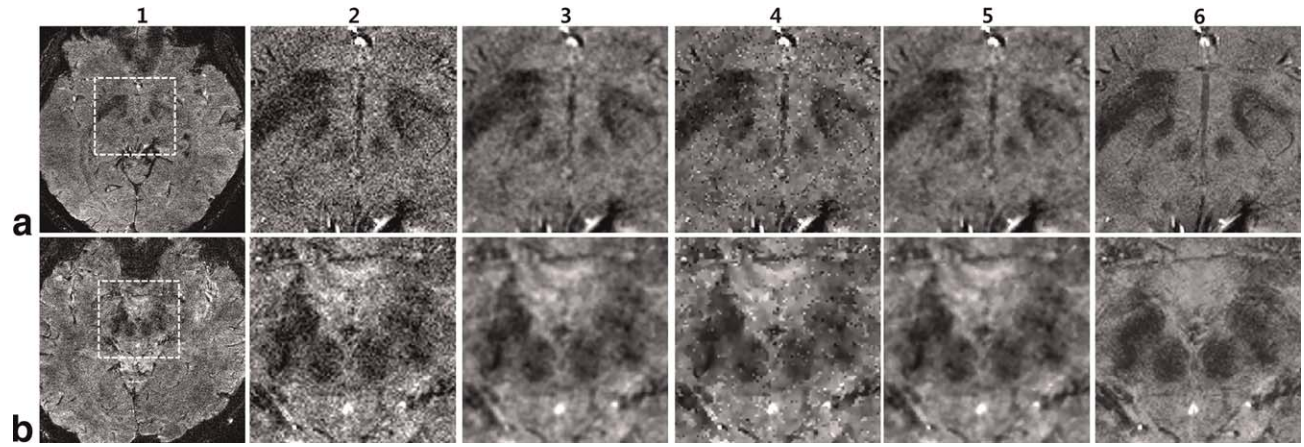

FIGURE 12: Denoised images at TE = 38.7 msec for subject 4 (row a) and subject 5 (row b). Left to right: original noisy images, magnified images of column 1, images denoised by LPF, ADF, bilateral filter, and proposed denoising method.

TABLE 4. STN/RN Conspicuity of Images in Fig. 12

	Original noisy	LPF	ADF	Bilateral	Proposed
Subject 4	7.2	7.0	7.4	7.4	9.0
Subject 5	6.8	8.0	7.2	7.8	9.2

the performance of the denoising method. Pixels of similar tissue characteristics can be measured as different tissues because of the field distortion-induced signal changes in multiecho MR data.[37–39] Consequently, this results in a reduction of the number of pixels for averaging and less SNR improvement. Other studies have also reported that SNR improvement of less dense pixels is reduced when nonlinear filters are used.[40–42] Moreover, to correct this reduction in SNR improvement, nonlinear filters that can adaptively set filtering parameters for each pixel have been presented.[40–42] They mainly use a histogram or statistical distribution of the pixel intensities to set adaptive filtering parameters. Thus, it would be possible to resolve this limitation by setting the threshold value adaptively based on the histogram or density of temporal signals. The other limitation is that the processing time of the current implementation is relatively long. On a standard 8 GB RAM desktop computer, MatLab requires 41 minutes 32 seconds to process 1024 × 1024 images with 16-echo datasets. However, because many of the calculations of our proposed algorithm can be parallelized, the processing speed would be highly accelerated by adoption of a parallel computing scheme.

Future work would include an automatic threshold optimization. Other nonlinear filters that can automatically set filtering parameters mainly use background noise level,[16] spatially varying noise level,[20,43] or image content.[44] In our study, we set the optimal threshold value based on CNR performance between GM and WM, which is related to tissue detectability.[45] Because CNR calculations need ROI selection for each tissue, the optimal threshold value could be automatically set if the brain segmentation process were automated. In this context, many studies on automatic tissue segmentation for MR brain images[46,47] could be adopted for threshold optimization. To further advance threshold optimization, it would be possible to use other no-reference image quality metrics, in addition to CNR, that are highly correlated with the subjective scores measured by radiologists.[30]

In conclusion, we acquired high-SNR and high-resolution T_2(*)-weighted brain images via fast multiecho acquisition followed by a denoising method based on tissue characteristics. The proposed denoising method effectively reduced the noise of multiecho images and retained brain structures with high conspicuity.

Acknowledgments

Contract grant sponsor: National Research Foundation of Korea (NRF) grant funded by the Korea government (MSIP); contract grant number: 2016R1A2B4015016

References

1. Hwang DS, Du YP. Improved myelin water quantification using spatially regularized non-negative least squares algorithm. J Magn Reson Imaging 2009;30:203–208.
2. Hwang D, Kim DH, Du Y.P. In vivo multi-slice mapping of myelin water content using T_2^* decay. NeuroImage 2010;52:198–204.
3. Laule C, Kozlowski P, Leung E, Li DK, Mackay AL, Moore GR. Myelin water imaging of multiple sclerosis at 7T: correlations with histopathology. NeuroImage 2008;40:1578–1580.
4. Kuhlpeter R, Dahnke H, Matuszewski L, et al. R_2 and R_2* mapping for sensing cell-bound superparamagnetic nanoparticles: In vitro and murine in vivo testing. Radiology 2007;245:449–457.
5. Wood JC, Enriquez C, Ghugre N, et al. MRI R_2 and R_2* mapping accurately estimates hepatic iron concentration in transfusion-dependent thalassemia and sickle cell disease patients. Blood 2005; 106:1460–1465.
6. Haacke EM, Xu Y, Cheng YCN, Reichenbach JR. Susceptibility weighted imaging (SWI). Magn Reson Med 2004;52:612–618.
7. Haacke EM, Mittal S, Wu Z, Neelavalli J, Cheng YCN. Susceptibility-weighted imaging: technical aspects and clinical applications, Part 1. Am J Neuroradiol 2009;30:19–30.
8. Jang U, Nam Y, Kim DH, Hwang D. Improvement of the SNR and resolution of susceptibility-weighted venography by model-based multiecho denoising. NeuroImage 2013;70:308–316.
9. Johansen-Berg H, Rushworth MFS. Using diffusion imaging to study human connectional anatomy. Annu Rev Neurosci 2009;32:75–94.
10. Lee J, van Gelderen P, Kuo LW, Merkle H, Silva AC, Duyn JH. T_2^*-based fiber orientation mapping. NeuroImage 2011;57:225–234.
11. Liu C, Li W. Imaging neural architecture of the brain based on its multiple magnetic response. NeuroImage 2013;67:193–202.
12. Tournier JD, Mori S, Leemans A. Diffusion tensor imaging and beyond. Magn Reson Med 2011;65:1532–1556.
13. Deichmann R, Josephs O, Hutton C, Corfield DR, Turner R. Compensation of susceptibility-induced BOLD sensitivity losses in echo-planar fMRI imaging. NeuroImage 2002;15:120–135.
14. Stenger VA, Boada FE, Noll DC. Three-dimensional tailored RF pulses for the reduction of susceptibility artifacts in T_2^*-weighted functional MRI. Magn Reson Med 2000;44:525–531.
15. McVeigh ER, Henkelman RM, Bronskill MJ. Noise and filtration in magnetic resonance imaging. Med Phys 1985;12:586–591.
16. Gerig G, Kubler O, Kikinis R, Jolesz F. Nonlinear anisotropic filtering of MRI data. IEEE Trans Med Imaging 1992;11:221–231.
17. Murase K, Yamazaki Y, Shinohara M, et al. An anisotropic diffusion method for denoising dynamic susceptibility contrast-enhanced magnetic resonance images. Phys Med Biol 2001;46:2713.
18. Perona P, Malik J. Scale-space and edge detection using anisotropic diffusion. IEEE Trans Pattern Anal Mach Intell 1990;12:629–639.
19. Tomasi C, Manduchi R. Bilateral filtering for gray and color images. In: Proc 6th IEEE Int Conf Comput Vis, Bombay; 1998. p 839–846.
20. Samsonov AA, Johnson CR. Noise-adaptive nonlinear diffusion filtering of MR images with spatially varying noise levels. Magn Reson Med 2004;52:798–806.

21. Buades A, Coll B, Morel JM. The staircasing effect in neighborhood filters and its solution. IEEE Trans Image Process 2006;15:1499–1505.
22. Griswold MA, Jakob PM, Heidemann RM, et al. Generalized autocalibrating partially parallel acquisitions (GRAPPA). Magn Reson Med 2002;47:1202–1210.
23. Cocosco CA, Kollokian V, Kwan RKS, Evans AC. Brainweb: Online interface to a 3D MRI simulated brain database. NeuroImage 1997;5: S425.
24. Kwan RKS, Evans AC, Pike GB. An extensible MRI simulator for post-processing evaluation. In: Visualisation in biomedical computing. Berlin, Heidelberg: Springer; 1996. p 135–140.
25. Collins DL, Zijdenbos AP, Kollokian V, et al. Design and construction of a realistic digital brain phantom. IEEE Trans Med Imaging 1998;17: 463–468.
26. Brown MA, Semelka RC. MRI: basic principles and applications, 4th ed. New York: John Wiley & Sons; 2010.
27. Buades A, Coll B, Morel JM. A non-local algorithm for image denoising. In: Proc IEEE Comput Soc Conf Comput Vis Pattern Recogn, San Diego; 2005;2:60–65.
28. Yaroslavsky, L, 1985. Digital picture processing — an introduction. New York: Springer; 1985. p 78–81.
29. Stanisz GJ, Odrobina EE, Pun J, et al. T_1, T_2 relaxation and magnetization transfer in tissue at 3T. Magn Reson Med 2005;54:507–512.
30. Chow LS, Paramesran R. Review of medical image quality assessment. Biomed Signal Process Control 2016;27:145–154.
31. Mittal A, Soundararajan R, Bovik AC. Making a "completely blind" image quality analyzer. IEEE Signal Process Lett 2013;20:209–212.
32. Bydder M, Du J. Noise reduction in multiple-echo data sets using singular value decomposition. Magn Reson Imaging 2006;24:849–856.
33. Deepa B, Sumithra MG. Comparative analysis of noise removal techniques in MRI brain images. In: Proc IEEE Int Conf Computat Intell Comput Res, Madurai; 2015. p 1–4.
34. Varghees VN, Manikandan MS, Gini R. Adaptive MRI image denoising using total-variation and local noise estimation. In: Proc IEEE Int Conf Adv Eng Sci Manag, Tamil Nadu; 2012. p 506–511.
35. Komiyama M, Yagura H, Baba M, et al. MR imaging: possibility of tissue characterization of brain tumors using T_1 and T_2 values. Am J Neuroradiol 1987;8:65–70.
36. Linfante I, Llinas RH, Caplan LR, et al. MRI features of intracerebral hemorrhage within 2 hours from symptom onset. Stroke 1999;30: 2263–2267.
37. Majumdar S, Orphanoudakis SC, Gmitro A, et al. Errors in the measurements of T_2 using multiple-echo MRI techniques. I. Effects of radiofrequency pulse imperfections. Magn Reson Med 1986;3:397–417.
38. Majumdar S, Orphanoudakis SC, Gmitro A, et al. Errors in the measurements of T_2 using multiple-echo MRI techniques. II. Effects of static field inhomogeneity. Magn Reson Med 1986;3:562–574.
39. Yablonskiy DA, Haacke EM. An MRI method for measuring T_2 in the presence of static and RF magnetic field inhomogeneities. Magn Reson Med 1997;37:872–876.
40. Paranjape RB, Rangayyan RM, Morrow WM. Adaptive neighborhood mean and median image filtering. J Electron Imaging 1994;3:360–367.
41. Debayle J, Pinoli JC. General adaptive neighborhood image processing. J Math Imaging Vis 2006;25:245–266.
42. Grazzini J, Soille P. Edge-preserving smoothing using a similarity measure in adaptive geodesic neighbourhoods. Pattern Recognit 2009;42: 2306–2316.
43. Manón JV, Coupé P, Martí-Bonmatí L, et al. Adaptive non-local means denoising of MR images with spatially varying noise levels. J Magn Reson Imaging 2010;31:192–203.
44. Yan R, Shao L, Liu L, et al. Natural image denoising using evolved local adaptive filters. Signal Process 2014;103:36–44.
45. Siewerdsen JH, Moseley DJ, Bakhtiar B, The influence of antiscatter grids on soft-tissue detectability in cone-beam computed tomography with flat-panel detectors. Med Phys 2004;31:3506–3520.
46. Fischl B, Salat DH, Busa E, et al. Whole brain segmentation: automated labeling of neuroanatomical structures in the human brain. Neuron 2002;33:341–355.
47. West J, Warntjes JB, Lundberg P. Novel whole brain segmentation and volume estimation using quantitative MRI. Eur Radiol 2012;22:998–1007.